Keyhole Formation and Thermal Fluid Flow-Induced Porosity during Laser Fusion Welding in Titanium Alloys: Experimental and Modelling

Chinnapat Panwisawas[1,*], Bama Perumal[1], R. Mark Ward[1], Nathanael Turner[2,3], Richard P. Turner[1], Jeffery W. Brooks[1], Hector C. Basoalto[1,*]

[1]School of Metallurgy and Materials, University of Birmingham, Birmingham B15 2TT, UK

[2]Manuafacturing Technology Centre Limited, Ansty Park, Coventry CV7 9JU, UK

[3]School of Mechanical and Manufacturing Engineering, Loughborough University, Leicestershire LE11 3TU, UK

Corresponding author: c.panwisawas@bham.ac.uk, h.basoalto@bham.ac.uk

Abstract

High energy-density beam welding, such as electron beam or laser welding, has found a number of industrial applications for clean, high-integrity welds. The deeply penetrating nature of the joints is enabled by the formation of metal vapour which creates a narrow fusion zone known as a "keyhole". However the formation of the keyhole and the associated keyhole dynamics, when using a moving laser heat source, requires further research as they are not fully understood. Porosity, which is one of a number of process induced phenomena related to the thermal fluid dynamics, can form during beam welding processes. The presence of porosity within a welded structure, inherited from the fusion welding operation, degrades the mechanical properties of components during service such as fatigue life. In this study, a physics-based model for keyhole welding including heat transfer, fluid flow and interfacial interactions has been used to simulate keyhole and porosity formation during laser welding of Ti-6Al-4V titanium alloy. The modelling suggests that keyhole formation and the time taken to achieve keyhole penetration can be predicted, and it is important to consider the thermal fluid flow at the melting front as this dictates the evolution of the fusion zone. Processing

induced porosity is significant when the fusion zone is only partially penetrating through the thickness of the material. The modelling results are compared with high speed camera imaging and measurements of porosity from welded samples using X-ray computed tomography, radiography and optical micrographs. These are used to provide a better understanding of the relationship between process parameters, component microstructure and weld integrity.

Keywords: Keyhole formation, Thermal fluid flow, Processing-induced porosity, Laser fusion welding, Titanium alloys

1. Introduction

Titanium-based alloys are used extensively in modern aero-engines, to produce a number of critical components, on account of their excellent structural properties particularly when judged on a density-corrected basis. However, such structural components often need high integrity welding methods for their fabrication. Thus, for the joining of complex components, traditional fusion welding techniques still hold considerable importance [1,2], as these processing routes allow for reasonable joint integrity. Fusion welding processes include the older-type arc-welding methods such as TIG, MIG and laser-arc hybrid welding [3-5], and newer beam-welding methods such as laser and electron-beam [6]. The beam processes enable the heat source to become more focused, allowing the molten pool region to form a narrower, deeper weld. These beam-welding applications have a higher power density compared to arc-weld processes. However although beam-welding applications such as laser welding are generally good for producing clean, high-integrity weld joints, any fusion welding operation must have associated distortions, and a probability of forming sub-surface defects such as porosity. The size and shape of the weld bead is clearly a critical output for

determining weld distortion, and this has been discussed in the literature in the context of validated modelling methods [7].

However, whilst distortions can be relieved with machining or post-weld heat treatments, defects such as porosity remain locked within the weld joint once the part has solidified [8]. Porosity defects can occur during the fusion welding processing due to various reasons. Silvinskii *et al.* [9] hypothesised that the presence of titanium hydride plays a large role in porosity formation. Later, the appearance of pores during the fusion welding of a titanium alloy was attributed to the presence of gas forming substances (oil, grease, moisture) on the surfaces being welded and therefore inadequate cleanliness levels [10]. Weld speed has also been found to correlate with porosity formation [11].

Huang *et al*.[12] have reported two distinct causes for the formation of defects in an electron beam weld; (i) that the electron beam source becomes fractionally offset from the butt-joint of the 2 parts, thus any remnant gas struggles to escape through the molten pool and in to the weld keyhole, where it can exit the weld entirely. And (ii) the level of hydrogen concentration within the base Ti-6Al-4V material has a considerable impact upon the porosity formation. Hydrogen migration during welding activities has also been studied in an attempt to rationalise the pore formation observed during beam welding applications [13]. Additionally, the morphology and size of the defect formed is believed to give an indication as to its formation mechanism; whereby a round pore of typically 100-300μm diameter, with a smooth inner surface, would suggest gas-formation (typically hydrogen related) [12,14].

The welding keyhole formed during a high-power density beam welding process is understood to be an unstable phenomenon, with the vapour keyhole shape and interface with the surrounding molten weld pool subject to constant changes as the vapour pressure causes the keyhole to momentarily close up, before re-forming and growing again. Establishing a

steady keyhole shape is believed to improve the cleanliness of the weld, reducing the probability of defect formation. The role played by the rapidly changing, undulating interface between the molten weld pool and the vapour keyhole is not well understood, but clearly any liquid / gas interface has a substantial potential for the formation of small gas bubbles or pores within a surrounding different phase.

Computational fluid dynamics (CFD) methods have recently been discussed within the literature [15-20] and applied to beam-welding methods such as laser welding, including the weld phenomena observed in experimental welds such as weld crown and toe formation, defect formation and the keyhole vapour phase present within the weld pool. In this work, we focus on using a validated CFD modelling method to understand better the mechanics occurring at the beginning of welding, during keyhole formation and within the fluid weld pool region, that lead to defect and porosity formation. This is to rationalise the formation of process induced porosity associated with the thermal fluid dynamics. Experimental trials were carried out using bead-on-plate welding as this excludes the possibilities of other sources of porosity from, for example, the surface roughness of two joints or beam offset. It is believed that hydrogen induced porosity will be relatively small due to the low hydrogen content in the alloys [14]. The CFD model is validated using this targeted experimentation and post weld analysis of the fusion zones to determine the presence, location and sizes of pore defects.

2. Experimental and Method

2.1 Modelling Methodology

The model was constructed and developed using the C++ open source code OpenFOAM® (Open Field Operation And Manipulation) toolbox, and uses a single material (metal) with multiple phases (solid, liquid and gas). It uses the standard balance of forces and conservation

of momentum and energy; it also includes reaction forces from vaporization, and Marangoni force, and the laser is applied as a volumetric heat source. It does not include momentum coupling between the vapour phase and other phases however. The model assumes that the Reynolds number of the molten liquid metal within the weld bead is sufficiently low such that a laminar solver is appropriate. Similar assumptions are made in other CFD modelling approaches for fusion welding [19-22]. The choice of representation of the laser interaction with the material is significant. A full optical model would be ideal, using the complex material refractive index and including interaction with the plasma. However the computational requirements are extreme [20] and there are unknowns concerning the plasma properties. An engineering approximation (e.g. [23]) is to represent the multiple reflections by a volumetric energy density. This pre-supposes some aspects of the nature of the solution, but is capable of being predictive over the range of cases presented in this paper. A brief summary of the theoretical framework used in simulating the weld pool dynamics during fusion welding has been given here. A detailed description of the approach is outlined by Panwisawas *et al.* [21]. The starting point is the usual assumption of material is incompressible expressed in terms of the continuity condition,

$$\boldsymbol{\nabla} \cdot \boldsymbol{u} = 0 \tag{1}$$

where, $\boldsymbol{u}$ is flow velocity. The computation domain is divided into a metallic α_1 region and atmospheric gaseous α_2 regions. The solid, liquid and vapour metal constitutive behaviours are defined within α_1 by introducing appropriate phase transformations depending on the temperature, being either below the solidus, between the solidus and liquidus temperature, above the liquidus temperature or above the vaporisation temperature. Above the vaporisation temperature, metal liquid transforms to metal vapour. The latter vapour phase is converted in to α_2. The summation of metallic α_1 and gaseous phases α_2 is always unity, i.e. $\alpha_1 + \alpha_2 = 1$, in every fluid element. Additionally, a weight function of any parameter x is used to smear

out the effect of metallic and gaseous phases, defined as, $\bar{x} = x_1\alpha_1 + x_2\alpha_2$. Modelling the dynamics of the weld pool is achieved by tracking the evolution of the α_1 and α_2 phases by a continuity condition with appropriate source/sink terms corresponding to phase transitions.

Thus, the volume occupied by the α_1 phase will evolve through the following differential equation,

$$\frac{\partial \alpha_1}{\partial t} + \boldsymbol{\nabla} \cdot (\alpha_1 \boldsymbol{u}) = -\frac{\dot{m}_V}{\rho_2} \quad (2)$$

where t is time, and the sink term in the right hand side (RHS) describes the loss of metallic phase due to evaporation when the evaporation temperature T_V is reached. In this work, ρ_2 is referred to the density of metal vapour which is no difference from atmospheric gas phase as chemical species is not distinguished here. The mass evaporation rate $\dot{m}_V$ is a function of the vapour recoil pressure p_V [17, 20, 25-26]. As reported previously in [27-28], the beginning of interaction between heat source and the materials predicts the kinetics of the melt pool. The governing field equation describing the flows of the liquid metal in weld pool and metal vapour is the Navier-Stokes equation,

$$\frac{\partial \bar{\rho}\boldsymbol{u}}{\partial t} + \boldsymbol{\nabla} \cdot (\bar{\rho}\, \boldsymbol{u} \otimes \boldsymbol{u}) = -\boldsymbol{\nabla} p + \boldsymbol{\nabla} \cdot \boldsymbol{T} + \boldsymbol{f}_{bouyancy} + \boldsymbol{f}_{melting} + \boldsymbol{f}_{surface} \quad (3)$$

where $\boldsymbol{T}$ is the viscous deviatoric stress tensor, p the hydrostatic pressure, and $\bar{\rho}$ is the density. Appearing on the right hand side of Equation (3) is a number of force terms. The buoyancy force term $\boldsymbol{f}_{bouyancy}$ is caused by density differences due to thermal expansion. $\boldsymbol{f}_{melting}$ is a damping force associated with the frictional dissipation in the mushy zone and given by Carman-Kozeny equation which is an enthalpy method for phase changes [29-30]. A number of mechanisms contribute to the surface force, $\boldsymbol{f}_{surface}$, which in the present treatment are the surface tension, Marangoni force and recoil vapour pressure. The Marangoni force is a thermo-capillary force that arises from temperature gradients across the

liquid/gas interface [24, 31-32]. All surface forces appearing in Equation (3) act only on the metal liquid/vapour interface. The conservation of total energy is written as

$$\frac{\partial \bar{\rho}\,\bar{C}_p T}{\partial t} + \boldsymbol{\nabla}\cdot\left(\bar{\rho}\,\boldsymbol{u}\,\bar{C}_p T\right) = -\frac{\partial \bar{\rho}\,\Delta H_f}{\partial t} - \boldsymbol{\nabla}\cdot\left(\bar{\rho}\,\boldsymbol{u}\,\Delta H_f\right) + \boldsymbol{\nabla}\cdot\left(\bar{k}\boldsymbol{\nabla}T\right) - \left[\left(h_c\left(T - T_{ref}\right) + \sigma_s\epsilon\left(T^4 - T_{ref}^4\right) + Q_V\right)|\boldsymbol{\nabla}\alpha_1| - Q_T\right]\frac{2\bar{C}_p\bar{\rho}}{\left(\bar{C}_{p1}\rho_1 + \bar{C}_{p2}\rho_2\right)} \quad (4)$$

The thermal energy is balanced between:

- heat input due to the heat source term Q_T (per unit volume), proposed by Xu et al. [23],

$$Q_T(r,z) = \frac{\zeta\eta q_{\text{laser}}}{\pi(1-e^{-3})(E+F)}\left(\frac{1-\chi}{z_e - z_i}z + \frac{\chi z_e - z_i}{z_e - z_i}\right)\exp\left(-\frac{3r^2}{r_0^2(z)}\right)$$

Note that the heat source term is a function of power distribution factor ζ, effective absorption factor η, total laser power q_{laser}, beam radius z_e

- heat loss due to conduction, $\boldsymbol{\nabla}\cdot\left(\bar{k}\boldsymbol{\nabla}T\right)$, convection, $h_c\left(T - T_{ref}\right)$, radiation, $\sigma_s\epsilon\left(T^4 - T_{ref}^4\right)$ and evaporation, $Q_V \sim \dot{m}_V \Delta H_V$ [33-34].

Here, $\bar{C}_p$ is specific heat for the mixture, $\bar{k}$ is thermal conductivity of the mixture, ΔH_f is the enthalpy change due to fusion, h_c is heat transfer coefficient, σ_s is Stefan-Boltzmann constant, and ϵ is emissivity. By solving the set of equations (1), (2), (3) and (4), the evolution of melt kinetics and liquid/gas interface change can be analysed and rationalised. A detailed model description is to be published elsewhere [27-28] and model parameters were adopted from [15-16, 35]. All modelling and heat source parameters are tabulated in Tables 1 and 2.

2.2 Welding experimentation

In this study, bead-on-plate laser welds were performed on 1 mm, 2 mm and 5 mm thick plates of Ti-6Al-4V titanium alloy using a Trumpf TruDisk laser system at the University of

Birmingham. This employs a fibre laser with a wavelength of ~ 1030nm and a beam spot size of ~800μm in diameter. The Ti-6Al-4V titanium alloy plates were purchased from Ti-Tek UK Ltd, Birmingham. The target chemical compositions in weight percentage of the Ti-6Al-4V alloy are shown in Table 3. The microstructure of the laser welded Ti-6Al-4V titanium alloy weld stripe was characterised to assess the structural integrity of the welds.

2.3 High speed camera imaging

High speed imaging was conducted using a Photron FASTCAM Mini UX100 high speed camera together with a Qioptiq long distance microscopic lens to develop understanding of the interaction between the laser beam and the Ti-6Al-4V. The imaging presented here was performed on 1mm thick plate at laser powers of 1000W, 2000W and 3000W, and under a constant weld speed of 100mm/s. The images were taken at 10000 frames/s.

2.4 X-ray radiography and tomography

To characterise the porosity of the laser welded Ti-6Al-4V weld stripe, the following non-destructive testing (NDT) methods were used; For a rapid investigation of large pore formation, conventional X-ray film radiography with resolution of 50 μm was performed on the laser welded Ti-6Al-4V plates (2 mm and 5 mm). This facility was made available to the researchers in the electron beam welding unit, Rolls-Royce plc, Derby, UK. The resolution of conventional X-ray radiography can approach around 2% of the thickness of the specimens. The advantage of X-ray radiography is the high efficiency for porosity detection in a large welded part, but there also some disadvantages, e.g. the overlap of pores and surface defects, and relatively low spatial resolution. Thus, to investigate further the three dimensional location and morphology of the porosity, X-ray computed tomography (CT) scanning analysis methods were performed to gain high resolution images and the precise three dimensional locations of the defects present within the Ti-6Al-4V laser weld stripe. This was

carried out using a Nikon XT H 225kV, with a reflection and transmission target of down to 3µm focal spot size, available at both the University of Birmingham and Manufacturing Technology Centre. It is note that the effective resolution for the Ti-6Al-4V material is about 50 µm when using an effective gauge volume of 5 × 2 × 10 mm^3, whereas the theoretical resolution for some very low density materials, (e.g. magnesium) can be as small as 3 µm (focal spot size) with the small gauge volume and small sample volume.

2.5 Material Characterisation

After locating the pores, the Ti-6Al-4V titanium alloy samples were sectioned and polished for metallurgical examination. Initially, the weld samples were cut using SiC (Silicon Carbide) cutting blades and the sectioned specimens were mounted under pressure using conductive powder for metallographic preparation. After mounting the samples were ground with Silicon Carbide (SiC) paper with grit sizes varying from 240 to 1200. After grinding, the samples were thoroughly washed with water and subsequently polished using a Struers MD largo disk with 9µm, 3µm, and 1µm Diamond paste suspensions. Finally, to reveal the microstructure the samples were final polished using an MD Chem disk and an Oxide Polishing Suspension (OPS). Etching was performed with 2 ml HF (Hydrofluoric acid), 6 ml HNO_3 (Nitric acid) and 92 ml of distilled water. The respective optical micrographs for each welding condition were captured and analysed using a Zeiss Axioskop 2 MAT Optical microscope facility.

3. Results

3.1 Weld Pool formation

The formation of the solid/liquid and liquid/gas interfaces is of critical importance during a fusion welding operation as these interface regions control whether melting occurs as a

surface source or a keyhole. The keyhole formation mechanism has been predicted using the CFD modelling and these models were validated by high speed camera imaging. During the bead-on-plate keyhole fusion welding, the applied laser beam heat source produced a localised volume with the high energy density required to cause melting and vaporisation of the material. As this molten pool grows in its size and depth, it approaches becoming fully penetrating through the thickness of the joint. Where the vaporisation of material occurs, the recoil pressure from the vaporised metal introduces a force upon the liquid metal. This imparts a deformation upon the molten region, and hence creates the vapour filled keyhole. Figure 1 shows the effect of total laser power for a constant 100mm/s weld speed. The differing nature of the reflection between the solid (diffuse) and liquid metal (specular) allows for the approximate solid/liquid interface to be captured using high speed photography methods, when the weld pool region is close to the edge of the weld plate in focus.

It can be seen that the time taken to reach the keyhole formation and hence a full penetration weld varies with the total laser power such that the higher the laser power, the shorter the time taken to achieve full penetration welding. In addition, Figure 1(a) shows the physical liquid/gas interface and the undulating motion of the interface is captured using high speed photography as seen in Videos (1) – (3). The CFD modelling predictions are in good agreement with the experiments for a range of welding conditions. The welding conditions shown in Figures 1(b) and 1(c) required a longer time to achieve weld penetration while the latter welds only achieve partial penetration as confirmed by optical images shown later.

The prediction and characterisation of the fusion zone boundary is of interest to industry and academia. The CFD model provides a predictive capability to allow for greater understanding of the weld pool dynamics and the subsequent sub-surface defect formation, if present. Figure 1 illustrates that for the 1 mm thickness weld and 100mm/s traveling speed, the 3000W and 2000W give rise to full penetration welds. However, the weld at 1000W did not achieve full-

penetration. Therefore, in order to rationalise the formation of the fusion zone and the conditions experienced as full-penetration is reached, additional bead-on-plate welds using laser powers of 1000W, 1300W, 1500W, 1750W and 2000W were performed to study the fusion boundary, see Figure 2. Figure 2(a) shows the weld pool taken, using high speed photography, after the first 5ms of welding when the pool was still close to the edge of the plate. The laser power clearly dictates the pool size and shape. This finding was supported by the metallurgical study and the characterisation of the weld bead fusion zone after welding, using optical microscopy as shown in Figure 2(b). The CFD model can predict the fusion zone reasonably as illustrated in Figure 2(c).

Thus far, the CFD modelling and high-speed photography experiments have demonstrated that the formation of the keyhole and subsequent fusion zone is dependent upon the process parameters including, the optical coupling, fluid dynamics and heat transfer. Figure 3 demonstrates the variations observed in the fusion boundaries and microstructure resulting from the different process conditions. Weld pool dimensions in terms of top surface width and weld depth have been used to compare the modelling and experiment. The conditions that cause the transition from a partial penetration to a full penetration weld pool can be explicitly inferred from Figure 3(a), i.e. the critical laser power to achieve full penetration is in the range of 1750 – 2000W for a 1mm thickness Ti-6Al-4V plate. The microstructure varied from an equiaxed grain morphology at lower laser powers to a columnar grain morphology when a higher laser power was used. Also, when the laser power was constant at 1000W and the welding speed varied from 100mm/s to 800mm/s, significantly shallower fusion zones were observed for the 400mm/s and 800mm/s cases, see Figure 3(b).

3.2 Weld Porosity formation

Weld integrity is not only a function of the grain microstructure within a solidified weld pool, but the process induced porosity also plays an important role. Welding trial experiments were conducted on a 1mm thick plate, and no sub-surface porosity at all was observed when analysing the 1mm thick welds using X-ray tomography. Figure 4 illustrates the 3D image construction from X-ray tomography of 1mm thick welds showing that no pores were detected for the welding conditions of 1000W, 2000W and 100 mm/s. Table 4 summarises the welding parameters used and whether porosity was observed for these conditions.

Results indicated that plate thickness has some effect on the porosity. Welding a 2mm thick plate at a constant 4000W laser power and three welding speeds (25mm/s, 50mm/s and 100mm/s) gave full penetration, in which the subsequent grain morphology together with fusion zone boundary position was dependent upon the welding speed. The faster the heat source travel speed, the narrower the resulting fusion zone and the smaller the grain size Figure 5(a). When using X-ray tomography, a sub-surface pore was observed in the 5mm × 10mm × 2mm gauge volume for the welding speeds of 25mm/s, as shown in Figure 5 and Table 4. It is obvious that the pore of size above 500 μm was observed in the 25mm/s sample due to the higher laser energy density promoting a larger weld pool which is more prone to sites of processing-induced porosity. This will be rationalised in the discussion section.

However, process-induced porosity was more frequently observed in the bead-on-plate welding of 5mm thick material. This may be because any vapour or gas formed and enclosed as the heat source passes by physically has further to travel through the thickness of the material to escape the plate surfaces. Using a 1400 W laser power with 16.9mm/s welding speed or a constant 4000W laser power with welding speeds of 25mm/s, 50mm/s and 100mm/s, porosity was observed in all welds, using optical and x-ray tomography as illustrated in Figure 6. It can be seen from Figure 6(a) that the transition from a partial

penetration weld bead to a full penetration weld occurs when increasing the power from 1400W to 4000W. For the three welds with 4000W power, the number of pores in a 5mm × 10mm × 5mm gauge volume decreased with increasing welding speed, as shown in Figure 6(b) and Table 5. A sharp, narrow weld bead was observed at 4000W laser power with the fastest travel speed of 100mm/s. The slower the heat source travels, the more heat energy dissipates in to the material locally. This can lead to a more complex system of fluid flow lines within the molten region and in turn allows pores to be trapped.

After metallographic analysis of the 2 and 5mm thick bead-on-plate welds, several pores were successfully located. The pores were mostly spherical in shape, distributed along the weld line, with diameters ranging from 0.38 – 1.16 mm. Analysing the 2 mm thick bead-on-plate welds with 4000W beam power, a large pore of approximately 0.83 mm in diameter was detected in the 25mm/s sample, whereas a smaller pore (about 0.38 mm) was observed in the 100mm/s sample.

For the 5mm thick plates, spherical pores with diameter of approximately 0.56-1.16 mm were found in the 16.9mm/s and 25mm/s travel speed samples. However, pores of diameter ranging from 0.66-0.93mm were observed in the 50mm/s travel speed sample of the 5 mm thick plate. Only a pore of 0.91mm in size was found in the 100mm/s travel speed sample of 5 mm thick plate. The largest pore information has been tabulated in Table 5.

To further investigate the thermal fluid flow induced porosity formation, laser welding was experimentally studied using different weld plate thicknesses, laser powers and traveling speeds. Radiography was used to measure the pore size and distribution in the weld zone, revealing pores at the welding conditions tabulated in Table 2 for both 2mm and 5mm thick titanium alloy plate. The radiography images are shown in Figures 7(a) and (b). Comparison of the porosity measurement between 3D X-ray tomography and radiography is presented in

Figure 7(c). It is believed that the random distribution of the porosity, which is caused by the thermal fluid flow, observed in the modelling is a real effect as similar behaviour can be seen in the radiographic results. Moreover, the incidence of porosity is exacerbated in thick plates and at low travel speed. Note that the difference in the pore size measurement in Figure 7(c) is believed to be because X-ray tomography is better suited to more accurate measurements of pore size. The resolution of this technique can be as fine as 5μm, although this is dependent upon the volume and density of material to be penetrated by the incident X-rays. For this experiment it is estimated that an effective resolution of approximately 50μm was observed. Whereas the X-ray radiography method is useful to locate the presence and location of pores, but has a poorer resolution and capability to accurately measure their dimension. As a consequence it can be seen that the tomography reveals the smaller pores while the radiography provides information on the larger cavities. However, the evidence is sufficient to suggest the presence of pores and the variation with process variables.

4. Discussion

The application of the model to a welding process is shown in Figure 8; it can be seen that the model predicts many features typical of welds.

When the energy density was very high, the flow behaviour within the fluid region was predicted to become unstable and to include recirculation. This was particularly observed at the rear portion of the weld pool, behind the keyhole. Porosity was sometimes predicted at the toe of the weld bead. Figures 8(a) and 8(b) show the top and bottom surface of the 1 mm thick plate using 4000 W and 100 mm/s welding conditions. The distribution of the pores can be visualised from the contour of the metallic-gaseous interface, see Figure 8(c). Both the periodic collapse of the keyhole and instabilities in flow surrounding it are thought to contribute to porosity. One of the possible mechanisms of porosity formation is a processing-

induced one. Without any trapped gas due to the surface roughness or dirt of different two metallic pieces or any chemical reactions of oxygen or hydrogen, the thermal fluid flow characteristic can induce a circulatory flow and balance with the surface tension in such a way that a gas bubble can be trapped at the interface of the keyhole during its rapid undulations and hence form a pore. It is also believed that Marangoni flow due to the high thermal gradient during the process is responsible for the re-circulation at the melting front [24]. This is supported by Figure 8(d) which shows cross-sections through a weld pool of the liquid/gas interfaces predicted by the CFD model.

Figure 9 shows the general predictive capability of the CFD model compared with the available experimentation in [14]. The x-ray tomography scan is consistent with the CFD modelling prediction, once the steady state condition is satisfied and solidification is reached. The temperature profile computed from the thermal fluid model has been mapped on the liquid/gas interface for comparison with the 3D x-ray tomography results. Note that the solidus and liquidus temperature for Ti-6Al-4V here are 1878K and 1928K, respectively. The CFD modelling has been able to represent an incomplete collapsed keyhole surface and pore distribution at the toe of the weld.

The lack of porosity in the 1-mm-thick samples was probably due to there being sufficient time for fluid forces to remove pores before solidification froze them into the solid. Figure 10 shows the flow velocity for a 1-mm-thick weld using a 2000W beam power with 100mm/s travel speed. It is believed that the circulatory flow at the bottom of the melting front (see arrow in Figure 10) is responsible for the creation and trapping of gas bubbles during the welding process. However, with increasing plate thickness, greater porosity was observed; this may have been because any trapped gas would have to travel further to reach the surface in these cases, allowing the molten pool to solidify before the pore can escape.

The CFD modelling predictions were further analysed to understand these results for 2 mm and 5 mm thickness plate welds. After the solidification front has passed by, in the case of the 1 mm weld plate using 2000 W laser power and 100 mm/s traveling speed, the model predicts no porosity (Figure 11(a)). However, when doubling the weld plate thickness to 2mm, and using a 4000W laser power with a 25mm/s traveling speed, a predicted pore of approximately 0.4 mm diameter can be found, as seen in Figure 11(b). The faster welding speed used for the 2 mm thick plate welds has given rise to a narrower fusion zone and has minimised the porosity occurrence. This is hypothesised to be because the energy density would be less and subsequently the melt flow is rather more stable with less possibility of a pore forming (Figure 11(c)). However, the 5mm plate weld with 16.9 mm/s weld speed led to a partially penetrating weld bead only, and as such porosity can become trapped inside the weld zone as the fusion zone is larger and as such exacerbates the tendency for pores to form. Thus the modelling results are consistent with the experimental information, in terms of the occurrence of porosity and the weld surface deformation. The effect of the process variables on porosity formation is summarised in the normalised processing diagram of thermal fluid flow induced porosity for laser fusion welding in Figure 12.

Conclusions

Keyhole and processing induced porosity formation during laser fusion bead-on-plate welding has been investigated in this work, using experimental and CFD modelling methods. The following specific conclusions can be drawn:

1. CFD modelling of laser fusion welding of titanium can predict both keyhole formation and the processing induced porosity associated with the thermal fluid dynamics. The model can be interrogated further to help in the analysis of the porosity formation.

2. The evolution of the liquid/gas interface during keyhole formation was observed using a high speed camera and modelling.

3. Process induced porosity is understood to be dependent upon three welding parameters: plate thickness, laser power and traveling speed. It is exacerbated by increased plate thickness and slower welding speeds.

4. The pore size was experimentally observed using x-ray tomography, optical microscopy and radiography. A reduced tendency for porosity formation was observed in the 1mm thick plates. However, pores have been detected in the 2mm and 5mm thick plates which were mostly spherical with diameters of 0.38 – 1.16 mm.

5. Unstable flow and/or the time required for pores to be removed versus the local solidification time are the keys to porosity formation.

6. Porosity prediction from the CFD model is consistent with the available targeted experimental results.

Acknowledgements

C.P., B.P., R.M.W., R.T., J.B. and H.B. would like to acknowledge support under the Centre for Advanced Simulation and Modelling ($CASiM^2$) collaborative project between Rolls-Royce plc, the Manufacturing Technology Centre (MTC), the University of Birmingham, part funded by the European Regional Development Fund (ERDF). The authors also thank Alistair Smith of Rolls-Royce plc for radiography measurement, David Chater of Metrology Lab, MTC for computed tomography (CT) scan, and Max Turner and Dr. Yu Lu of University of Birmingham for x-ray tomography measurement.

References

[1] S. A. David, T. Debroy, "Current issues and problems in welding science," Science,

257 (1992) 497-502.

[2] T. DebRoy, S. A. David, "Physical processes in fusion welding," Reviews of Modern Physics, 65 (1995) 85-111.

[3] J.J. Blecher, T.A. Palmer, T. DebRoy, "Porosity in Thick Section Alloy 690 Welds - Experiments, Modeling, Mechanism, and Remedy," Welding Journal, 95(1) (2016) 17s-26s.

[4] H.L. Wei, J.J. Blecher, T.A. Palmer, T. DebRoy, "Fusion Zone Microstructure in Full Penetration Laser-Arc Hybrid Welding of Low Alloy Steel", Welding Journal, 94 (2015) 135s-144s.

[5] J.J. Blecher, T.A. Palmer, T. DebRoy, "Mitigation of Root Defect in Laser and Hybrid Laser-Arc Welding", Welding Journal, 94 (2015) 73s-82s.

[6] J.J. Blecher, C.M. Galbraith, C. Van Vlack, T.A. Palmer, J.M. Fraser, P.J.L. Webster, T. DebRoy, "Real Time Monitoring of Laser Beam Welding Keyhole Depth by Laser Interferometry," Science and Technology of Welding and Joining, 19 (2014) 560-564.

[7]. R. Turner, J-C. Gebelin, R.M. Ward, J. Huang, R.C. Reed, "Modelling of the Electron Beam Welding of a Titanium Aeroengine Compressor Disc," *Proceedings for 8th International Trends in Welding Research, Chicago* (2012).

[8] J.J. Blecher, T.A. Palmer, and T. DebRoy, "Solidification Map of a Nickel Base Alloy," Metallurgical and Materials Transactions A, 45A (2014) 2142-2151.

[9] V.A. Silvinskii, et al., "Role of hydrides in pore formation in welding titanium," Paton Welding Journal, 6 (1994) 265–269.

[10] N. Gouret, E. Ollivier, G. Dour, R. Fortunier, B. Miguet, "Assessment of the origin of porosity in electron-beam-welded TA6V plates," Metallurgical and Materials Transactions A, 35A (2004) 879–889.

[11] T. Mohandas, D. Banerjee, and V.V. Rao, "Fusion zone microstructure and porosity in electron beam welds of an α+β titanium alloy," Metallurgical and Materials Transactions A, 30(3) (1999) 789-798.

[12] J.L. Huang, R. Turner, J-C. Gebelin, N. Warnken, M. Strangwood, R.C. Reed, " The Effect of Hydrogen on Porosity Formation during Electron Beam Welding of Titanium Alloys," *Proceedings for 8th International Trends in Welding Research, Chicago* (2012).

[13] J.L. Huang, N. Warnken, J.-C. Gebelin, M. Strangwood, R.C. Reed, "Hydrogen Transport and Rationalization of Porosity Formation during Welding of Titanium Alloys," Metallurgical and Materials Transaction A, 42(2) (2012) 582–591.

[14] J.L. Huang, N. Warnken, J. C. Gebelin, M. Strangwood, R. C. Reed, "On the mechanism of porosity formation during welding of titanium alloys," Acta Mater. 60 (2012) 3215–3225.

[15]. R. Rai, J.W. Elmer, T.A. Palmer, T. DebRoy, Heat transfer and fluid flow during keyhole mode laser welding of tantalum, Ti-6Al-4V, 304L stainless steel and vanadium, J. Phys. D: Appl. Phys. 40 (2007) 5753–5766.

[16] R. Rai, P. Burgardt, J.O. Mileewski, T.J. Lienert and T. DebRoy, Heat transfer and fluid flow during electron beam welding of 21Cr-6Ni-9Mn steel and Ti-6Al-4V alloy, J. Phys. D: Appl. Phys. 42 (2009) 025503(12pp).

[17]. M. Geiger, K.-H. Leitz, H. Kock, A. Otto, A 3D transient model of keyhole and melt pool dynamics in laser beam welding applied to the joining of zinc coated sheets, Prod. Eng. Res. Devel. 3(2009) 127–136.

[18]. R. Fabbro, K. Chouf, "Keyhole modeling during laser welding," J. Appl Phys, 87(9) (2000) 4075–4082.

[19]. W. Tan, N.S. Bailey, Y.C. Shin, "Investigation of keyhole plume and molten pool based on a three-dimensional dynamic model with sharp interface formulation," J. Phys D: Appl Phys. 46 (2013) 055501.

[20]. M. Courtois, M. Carin, P. Le Masson, S. Gaied, M. Balabane, "A new approach to compute multi-reflection of laser beam in a keyhole for heat transfer and fluid flow modelling in laser welding," J. Phys D: Appl Phys., 46 (2013) 505305(14pp).

[21] C. Panwisawas, Y. Sovani, R.P. Turner, J.W. Brooks, H.C. Basoalto, H. Nilsson, H. Jasak, I. Choquet, "Physics-based keyhole modelling of laser fusion welding in titanium alloys: Keyhole dynamics, thermal fluid flow, and porosity formation," Submitted.

[22] I. Choquet, A.J. Shirvan, H. Nilsson, "On the choice of electromagnetic model for short high-intensity arcs, applied to welding," J. Phys. D: Appl. Phys. 45 (2012) 205203 (14pp)

[23] G.X. Xu, C.S. Wu, G.L. Qin, X.Y. Wang, S.Y. Lin, "Adaptive volumetric heat source models for laser beam and laser + pulsed GMAW hybrid welding processes," Int J Adv Manuf Technol 57 (2011) 245–255.

[24] L. E. Scriven, C. V. Sternling, "The Marangoni effects," Nature, 187 (1960) 186-188.

[25] X. Jin, L. Li, Y. Zhang, "A study on Fresnel absorption and reflections in the keyhole in deep penetration laser welding," J. Phys. D: Appl. Phys. 35 (2002) 2304–2310.

[26] X. Jin, P. Berger, T. Graf, "Multiple reflections and Fresnel absorption in an actual 3D keyhole during deep penetration laser welding," J. Phys. D: Appl. Phys. 39 (2006) 4703–4712.

[27] C. Panwisawas, C.L. Qiu, Y. Sovani, J.W. Brooks, M.M. Attallah, H.C. Basoalto, "On the role of thermal fluid dynamics into the evolution of porosity during selective laser melting," Scr. Mater. 105 (2015) 14 – 17.

[28] C.L. Qiu, C. Panwisawas, R.M. Ward, H.C. Basoalto, J.W. Brooks, M.M. Attallah, "On the role of melt flow into the surface structure and porosity development during selective laser melting," Acta Mater. 96 (2015) 72 – 79.

[29] V.R. Voller, M. Cross, N.C. Markatos, "An enthalpy method for convection/diffusion phase change," Int. J. Num. Meth. Eng. 24 (1987) 271 - 284.

[30] F. Rösler, D. Brüggemann, "Shell-and-tube type latent heat thermal energy storage: numerical analysis and comparison with experiments," Heat Mass Transfer 47 (2011) 1027–1033.

[31] T. Ytrehus, S. Østomo, "Kinetic theory approach to interphase processes," Int. J. Multiphase Flow 22 (1996) 133–155.

[32] H. Ki, P.S. Mohanty, J. Mazamder, "Modelling of high-density laser-material interaction using fast level set method," J. Phys. D: Appl. Phys. 34 (2001) 364–372.

[33] Y. Sun, C. Beckermann, "Diffuse interface modelling of two-phase flows based on averaging mass and momentum equations**,"** Physica D 198 (2004) 281–308.

[34] J.U. Brackbill, D.B. Kothe, C. Zemach, "A continuum method for modelling surface tension," J. Comp. Phys. 100 (1992) 335–354.

[35] J.Z. Li, W.L. Johnson, W.K. Rhim, "Thermal expansion of liquid Ti-6Al-4V measured by electrostatic levitation," Appl. Phys. Lett. 89 (2006) 111913(2pp).

Figure(s)

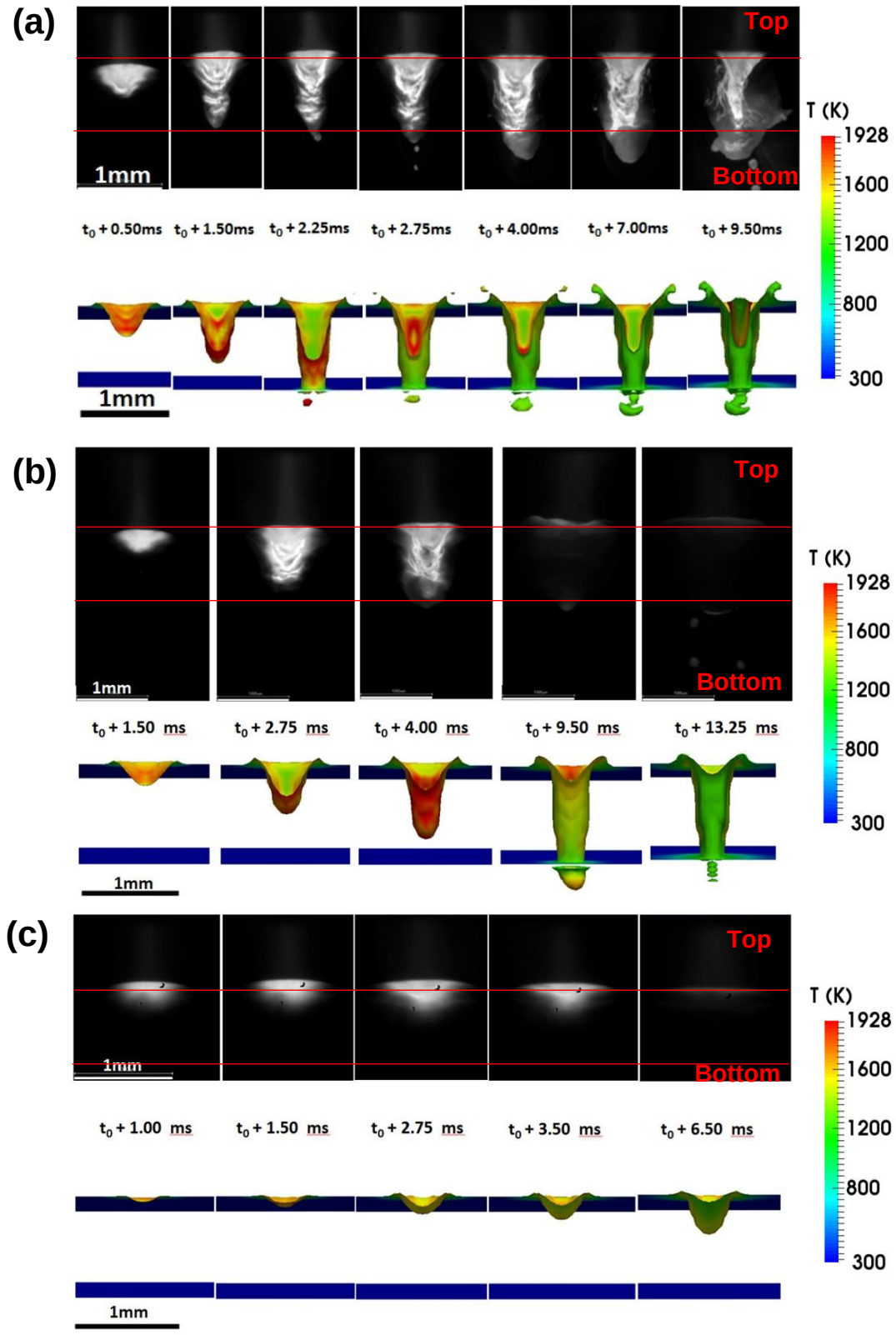

Figure 1: Comparison of liquid/solid interface during keyhole formation between modelling and high speed camera imaging using 100mm/s welding speed and (a) 3000W, (b) 2000W and (c) 1000W. Note that t_0 refers to initial time at which the laser contacts the weld plate, i.e. (a) t_0 = 2.75ms, (b) t_0 = 2.50ms, (c) t_0 = 2.00ms.

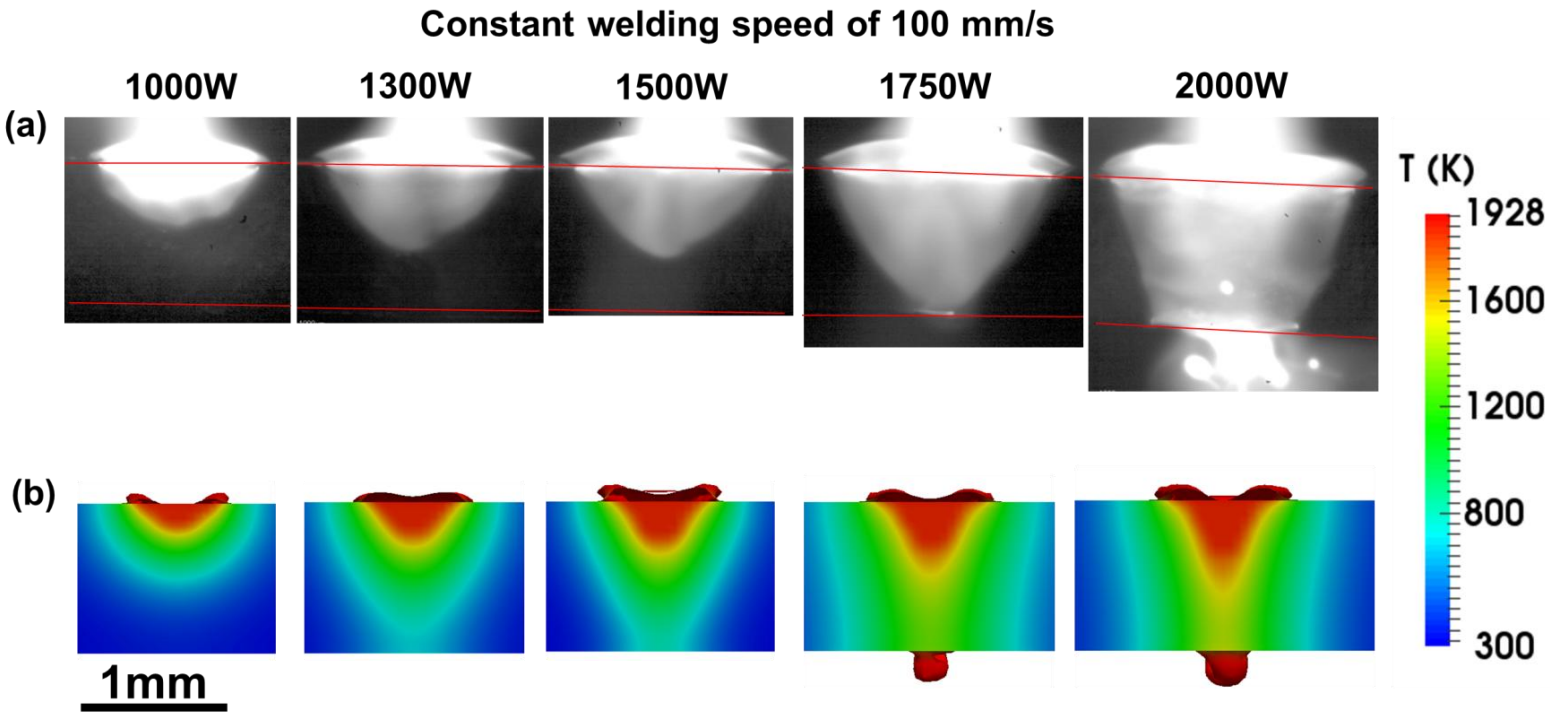

Figure 2: Comparison of in-situ fusion zone size and shape, viewed from the plate-edge, after 5ms welding using (a) high speed camera imaging, and (b) predicted fusion zone boundaries at the constant welding speed of 100 mm/s and 1mm thick weld plate with total laser power of 1000W, 1300W, 1500W, 1750W and 2000W.

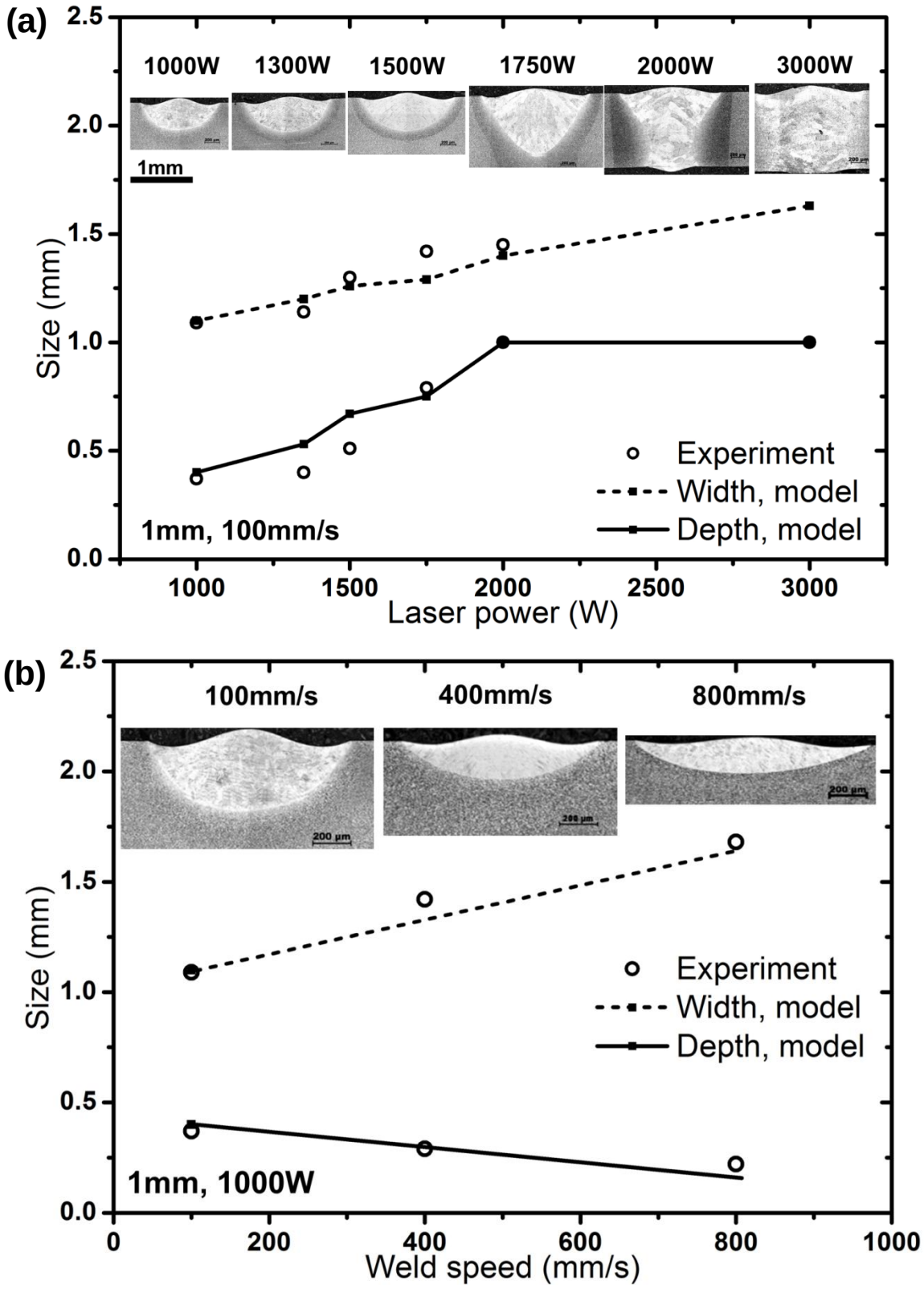

Figure 3: Comparison of experiment and model results for a 1mm thick weld varying two processing parameters: (a) laser power of 1000W, 1300W, 1500W, 1750W, 2000W and 3000W with constant welding speed of 100mm/s, and (b) welding speed of 100mm/s, 400mm/s and 800mm/s with the constant laser power of 1000W.

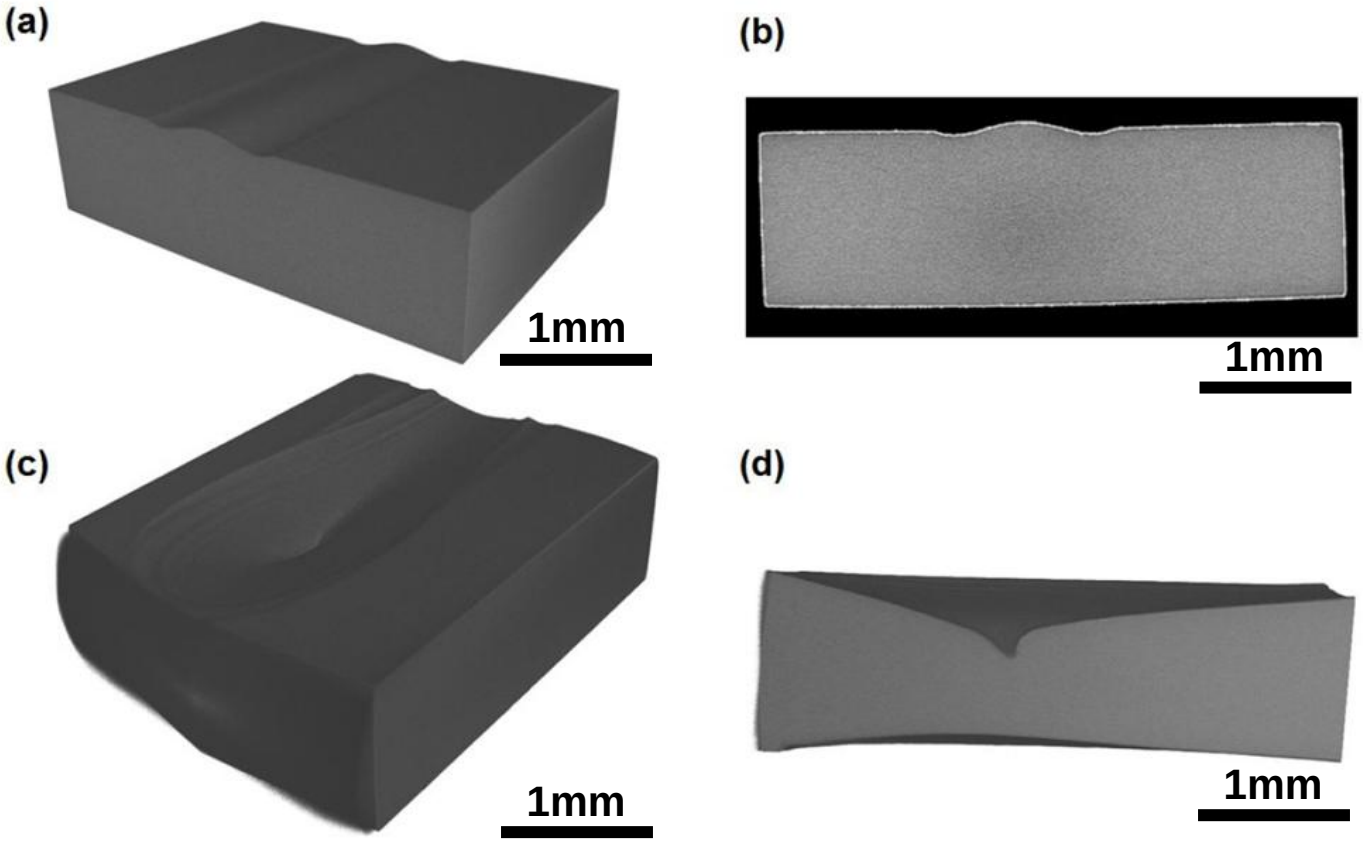

Figure 4: Reconstructed image from X-ray tomography: (a) a 1mm thick weld with 1000 W and 100 mm/s, (b) cross-sectional area of (a), (c) a 1mm thick weld with 2000W and 100 mm/s, (d) the longitudinal section of (c). NB there is no porosity visible in these images.

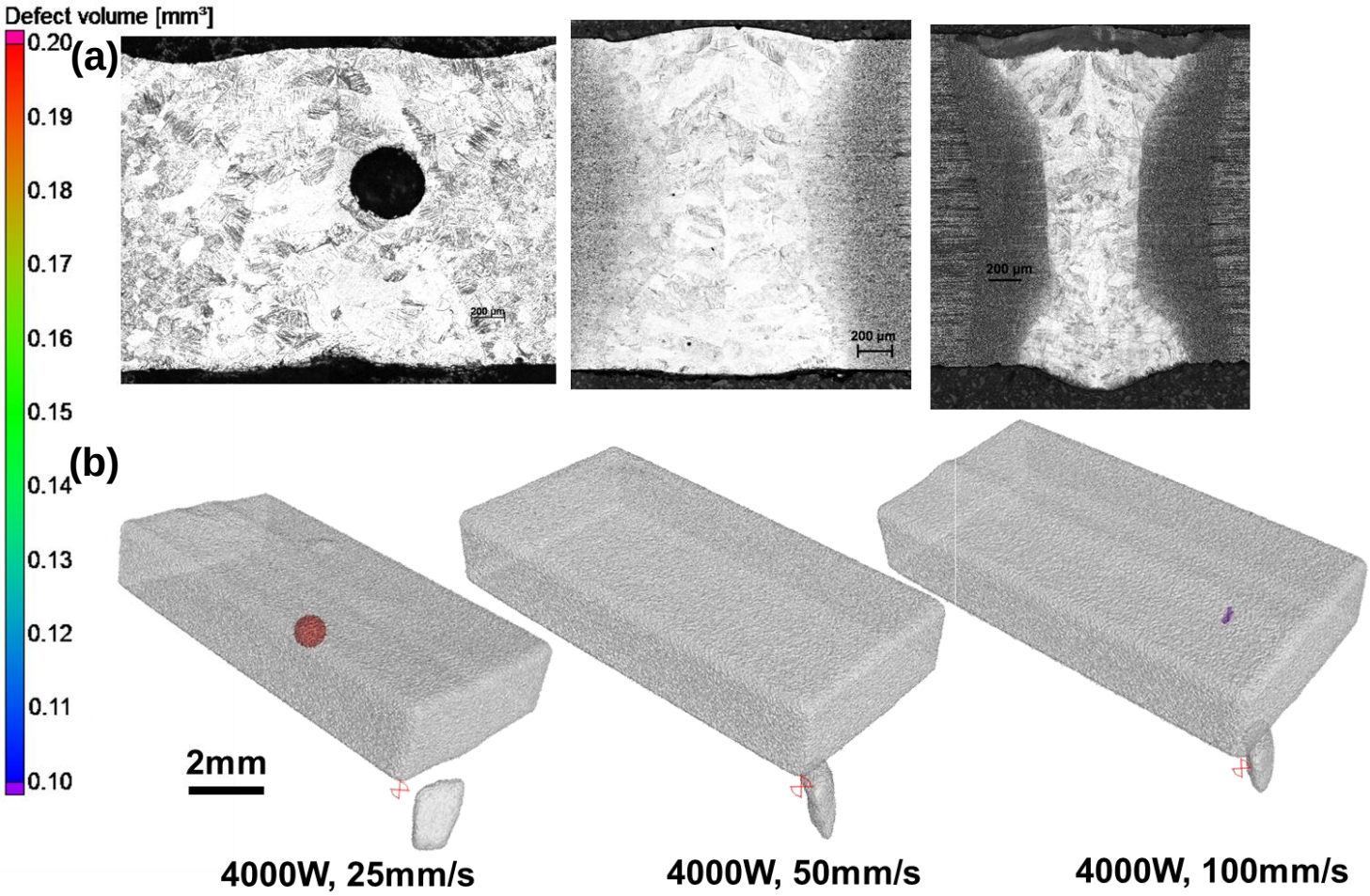

Figure 5: (a) optical micrographs and (b) reconstructed 3D X-ray tomography of the 2mm thick weld using welding conditions of a constant 4000W laser power and three welding speeds of 25mm/s, 50mm/s and 100mm/s.

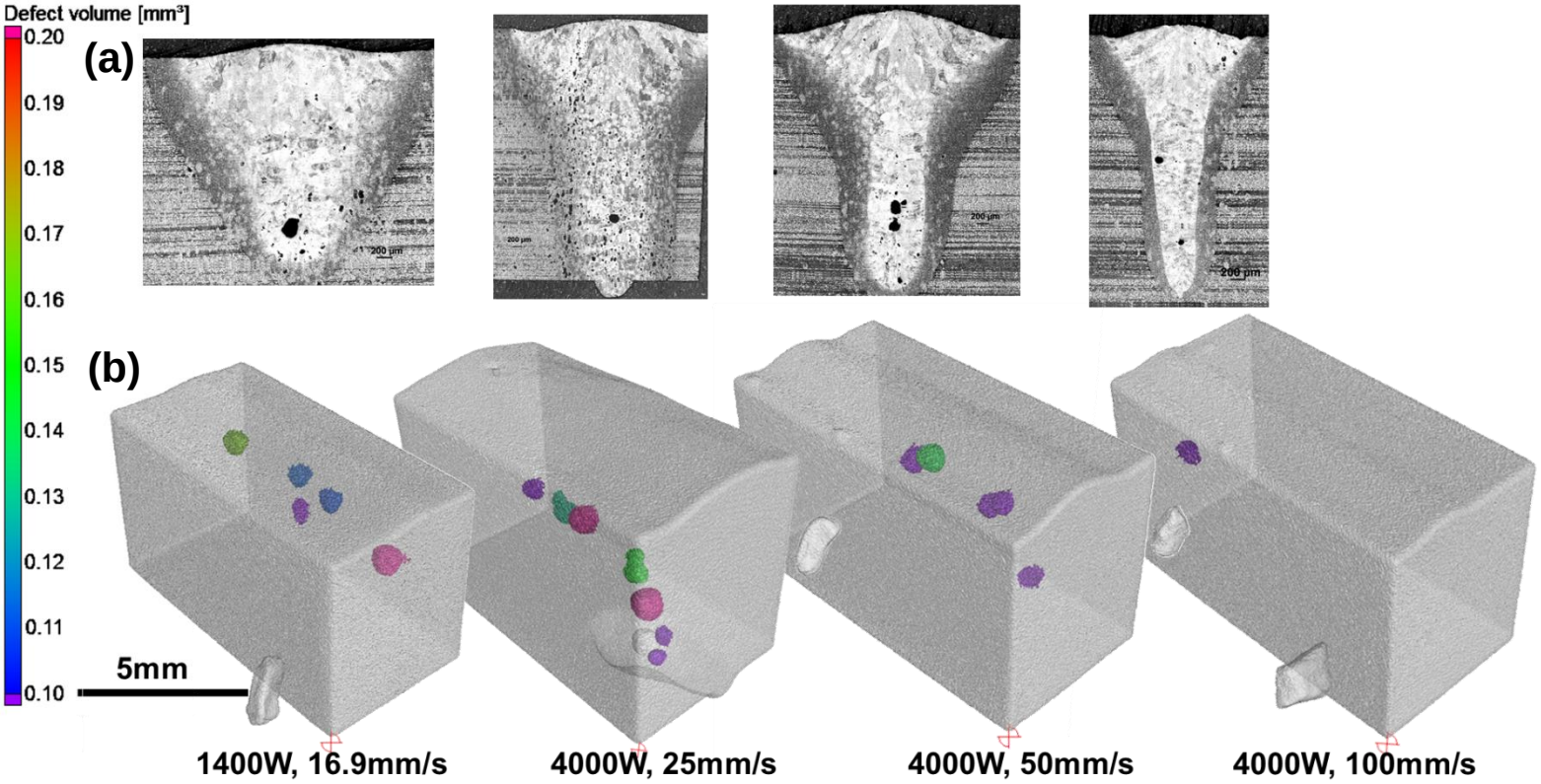

Figure 6: (a) optical micrographs and (b) reconstructed 3D x-ray tomography of the 5mm thick weld using the welding conditions of a 1400 W laser power weld with 16.9mm/s welding speed, and constant 4000W laser power welds with three welding speeds at 25mm/s, 50mm/s and 100mm/s.

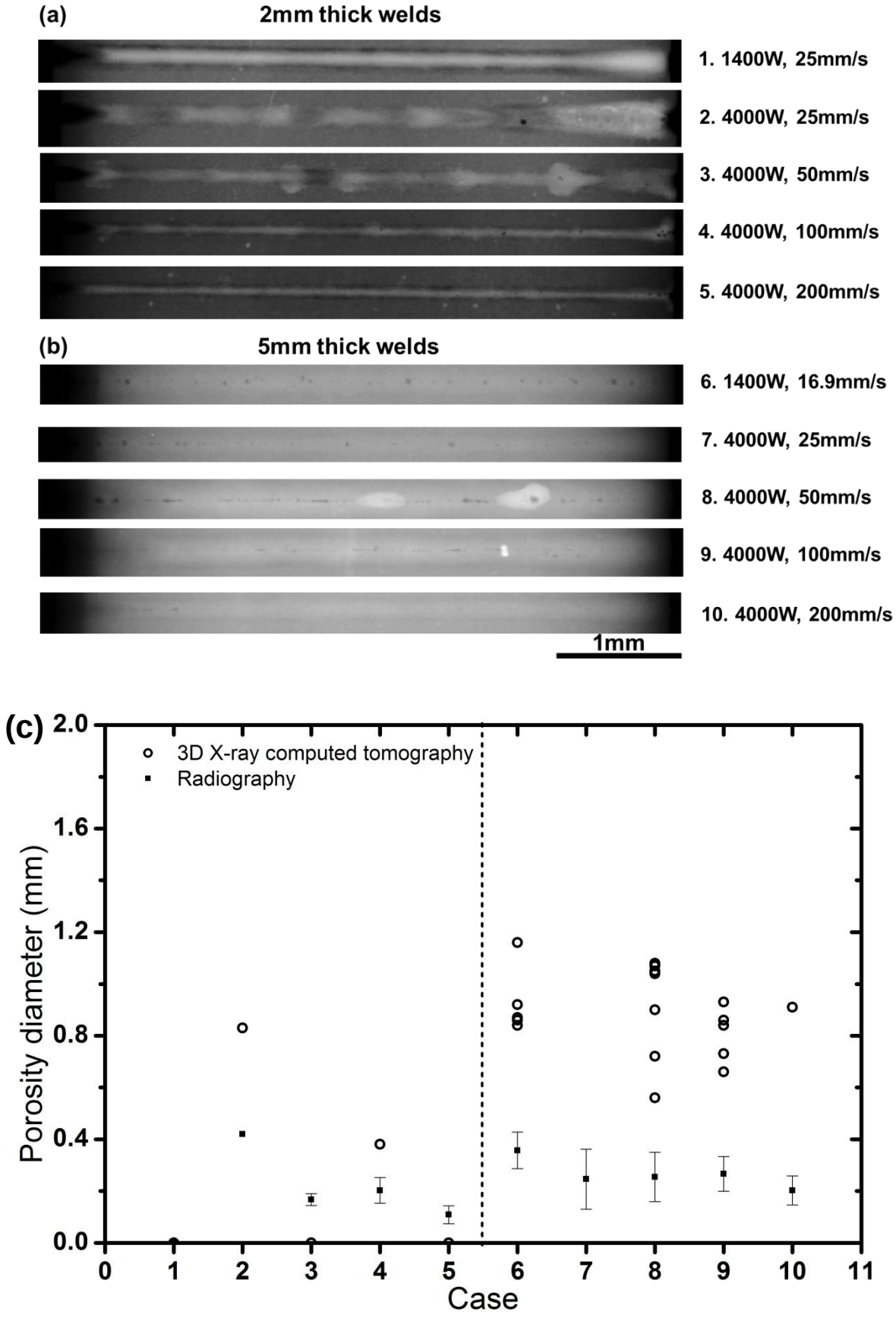

Figure 7: Radiography results showing the pore distribution along the weld for 2 plate thicknesses: (a) 2mm thick plate, (b) 5mm thick plate, and (c) the comparison between the porosity measurement using x-ray tomography and radiography.

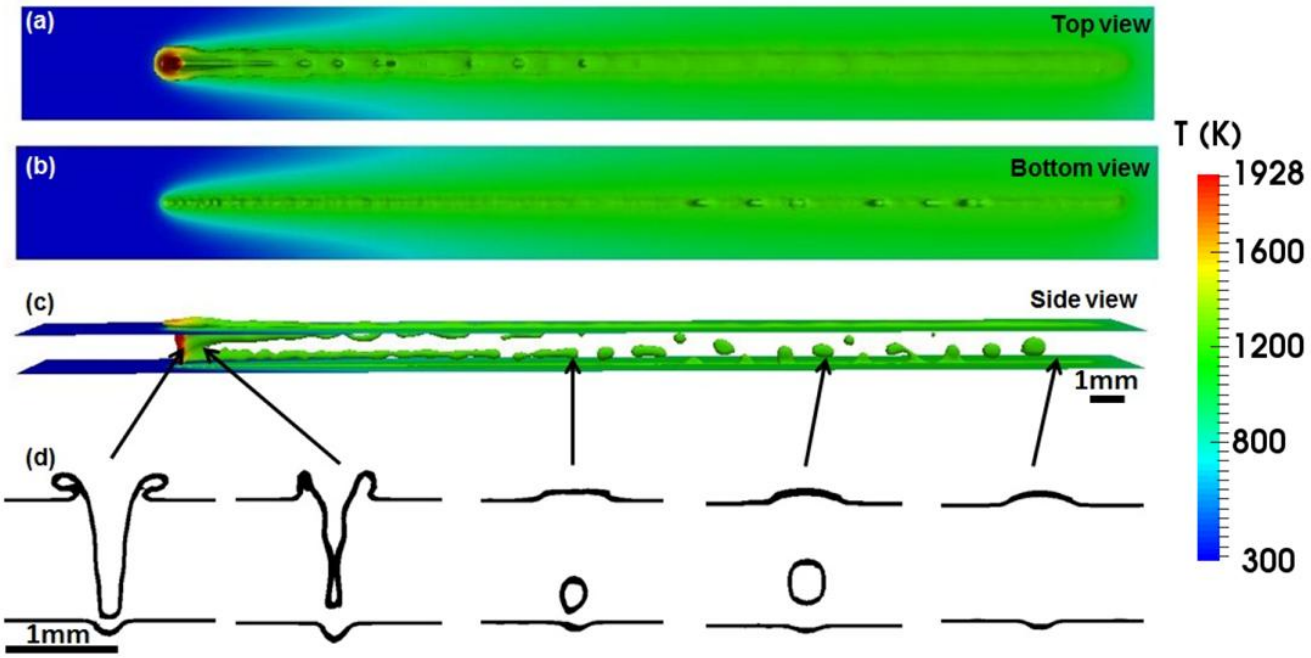

Figure 8: The metallic-gaseous interface plot of a 1mm thick weld plate with 4000W laser power and 100mm/s welding speed computed using the keyhole model proposed by [14]: (a) predicted top layer of the weld surface, (b) predicted bottom layer of the weld surface, (c) predicted longitudinal view of the weld, (d) predicted cross-sectional view along the weld line.

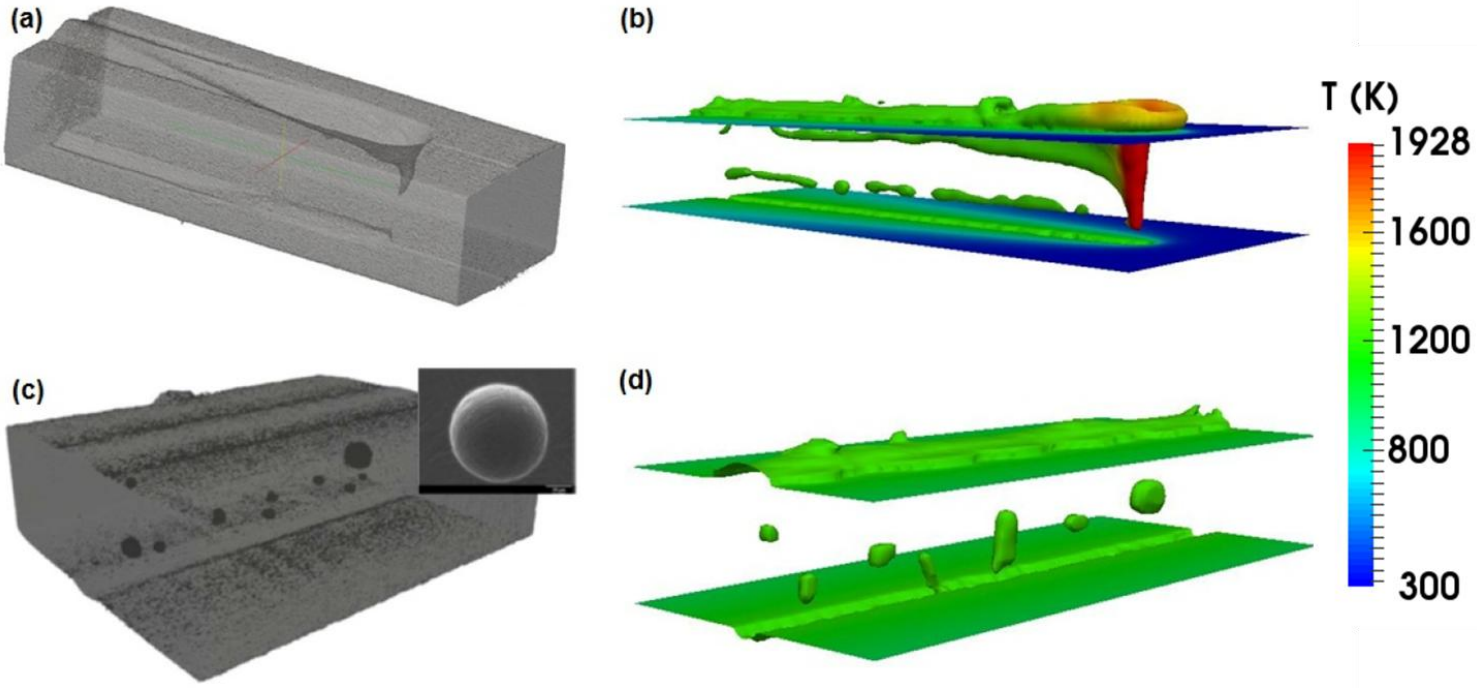

Figure 9: Comparison between (a) a partially collapsed keyhole surface using the reconstructed 3D X-ray tomography, after [14], and (b) keyhole modelling prediction of the liquid/vapour interface with 1mm thickness, 4000W and 100mm/s captured at the melting front, and between (c) pore distribution inside the weld bead reconstructed from X-ray tomography and (d) porosity prediction at the same condition as (b) but after solidification.

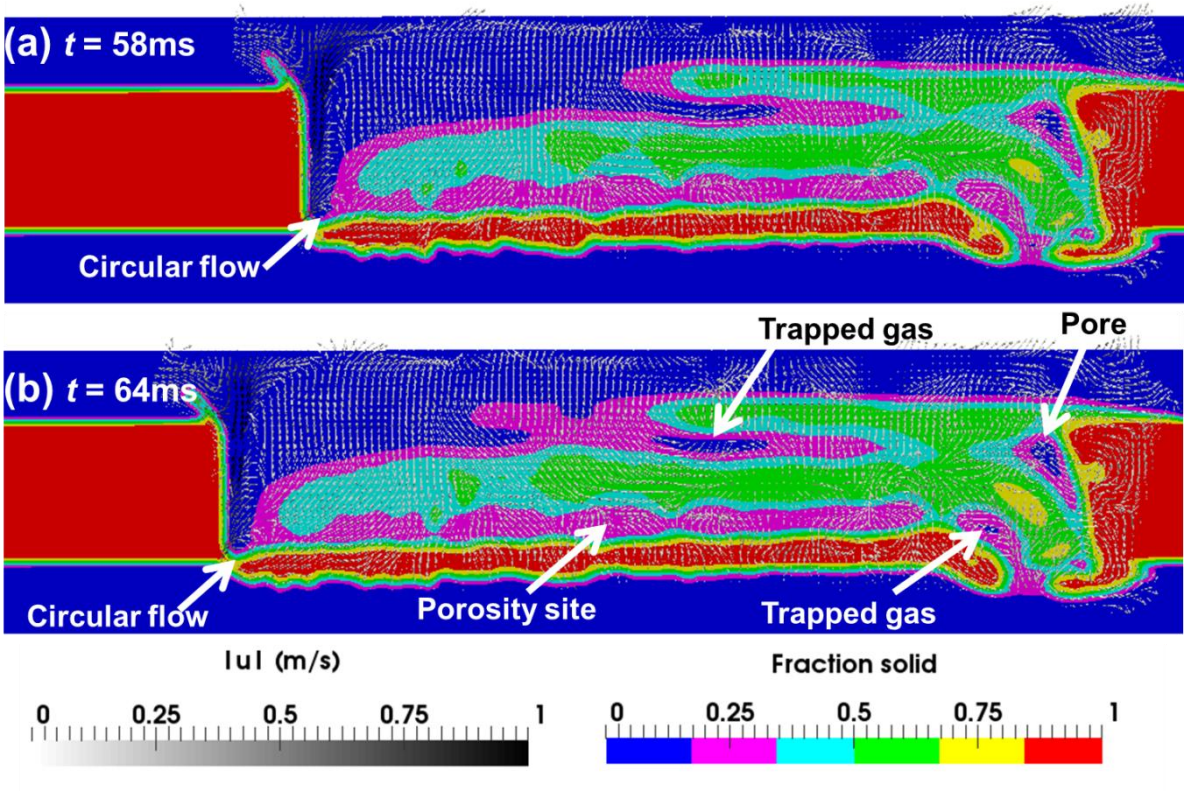

Figure 10: Velocity field and fraction of solid results from thermal fluid flow calculation comparing 2 instantaneous time intervals at (a) 58ms and (b) 64ms.

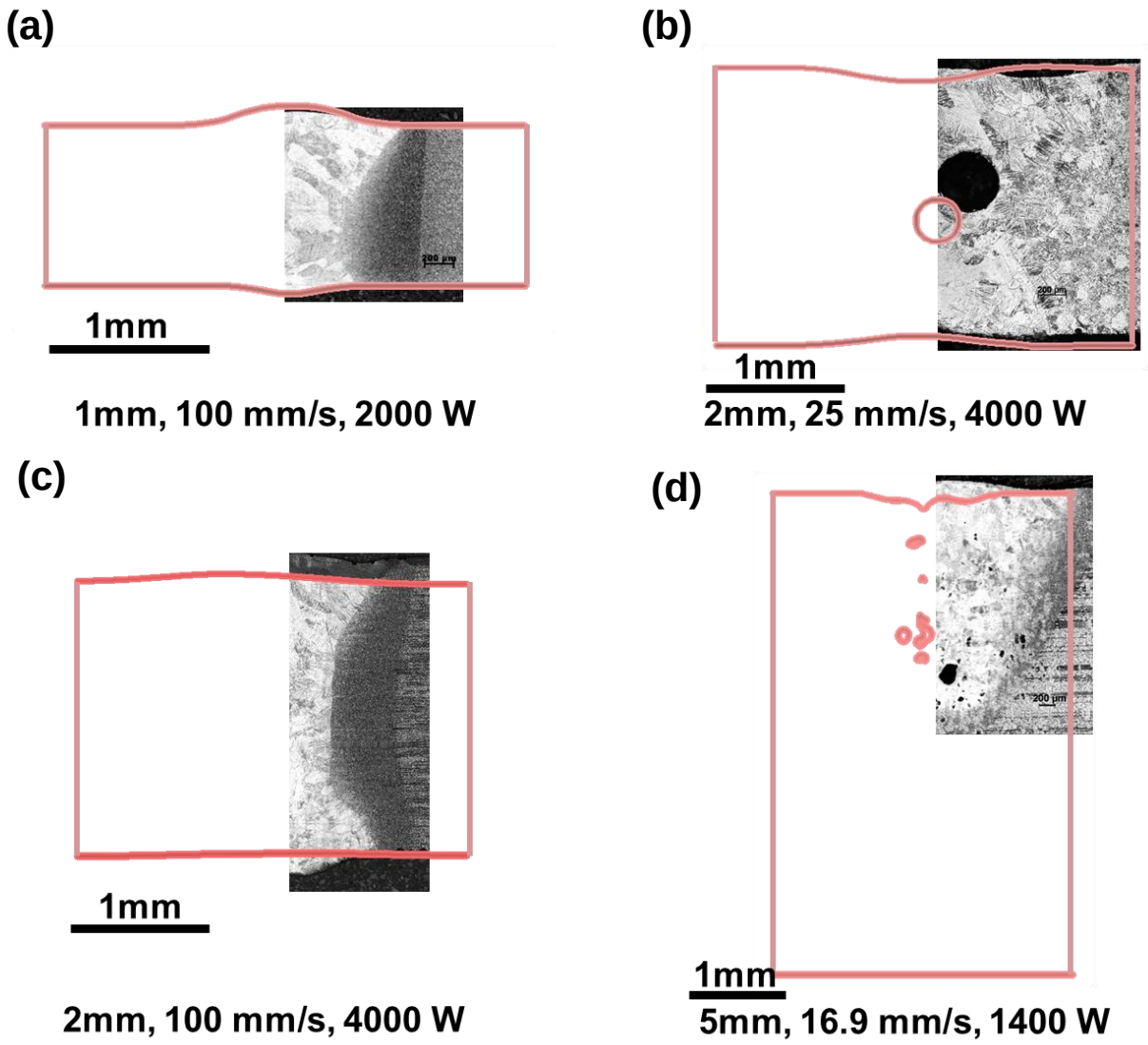

Figure 11: Comparison between outline of solid fraction profile (in red solid line) calculated using CFD and as-weld micrographs for four welding conditions: (a) 1mm thick plate with 100mm/s and 2000W, (b) 2mm thick plate with 25mm/s and 4000W, (c) 2mm thick plate with 100mm/s and 4000W, and (d) 5mm thick plate with 16.9mm/s and 1400W.

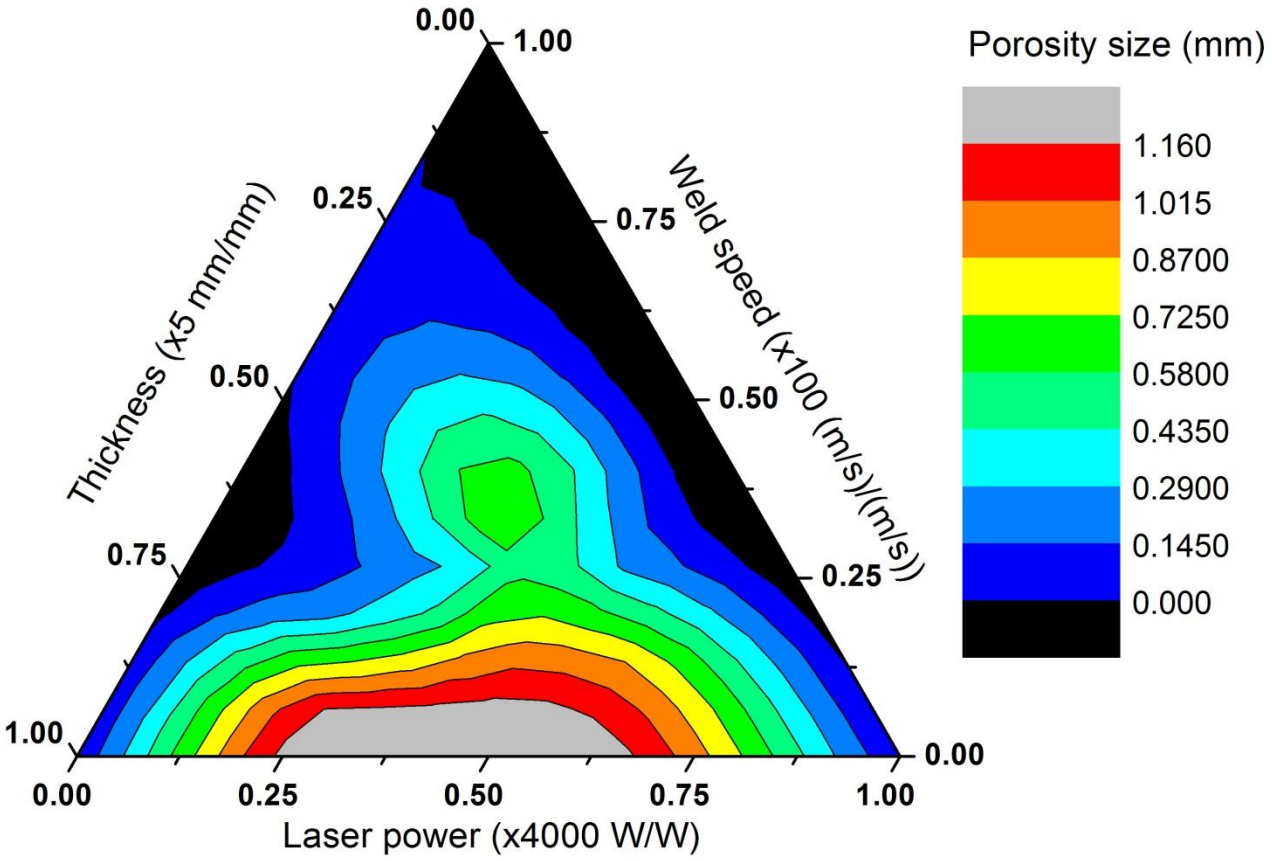

Figure 12: Normalised processing diagram of thermal fluid flow induced porosity for laser fusion welding, reporting maximum size of porosity.

Table 1: Data used for fluid flow and heat transfer calculations.

Physical properties	Ti-6Al-4V
Solidus temperature, (K)	1878
Liquidus temperature, (K)	1928
Evaporation temperature, (K)	3133
Density of liquid metal, ($kg.m^{-3}$)	4000
Molar mass, (g/mol)	446.07
Specific heat of solid metal, ($J\ kg^{-1}\ K^{-1}$)	670
Specific heat of liquid metal, ($J\ kg^{-1}\ K^{-1}$)	730
Thermal conductivity of solid metal, ($Wm^{-1}\ K^{-1}$)	21
Thermal conductivity of liquid metal, ($Wm^{-1}\ K^{-1}$)	29
Viscosity, (Pa.s)	0.005
Thermal expansion coefficient, (K^{-1})	8×10^{-6}
Surface tension, (Nm^{-1})	1.4
Temperature coefficient of surface tension, ($Nm^{-1}K^{-1}$)	-0.26×10^{-3}
Enthalpy of solid at melting point, ($J\ kg^{-1}$)	1.12×10^{6}
Enthalpy of liquid at melting point, ($J\ kg^{-1}$)	1.49×10^{6}
Enthalpy change of evaporation, ($J\ kg^{-1}$)	4.7×10^{6}
Atmospheric pressure, (Nm^{-2})	101300
Ideal gas constant, ($JK^{-1}\ mol^{-1}$)	8.314
Boltzmann's constant, ($J\ K^{-1}$)	1.38×10^{-24}

Table 2: Data used for heat source model in this calculation.

Heat source model parameters	Value
Power distribution factor	3.0
Total beam power, (W)	400
Effective absorption coefficient	0.24
Beam radius, (μm)	50
Beam velocity, (mm s^{-1})	16.9, 25, 100

Table 3: Chemical composition range of the Ti-6Al-4V alloy used in this study (weight percentage)

Alloy	**Ti**	**Al**	**V**	**C**	**Fe**	**O**	**N**
Ti-6Al-4V	Bal.	5.50-6.75	3.50-4.50	0.08	0.30	0.20	0.05

Table 4: Welding conditions used in the porosity study.

Plate thickness (mm)	**Laser power (W)**	**Traveling speed (mm/s)**	**Porosity**	**Weld pool geometry**			
				Weld width (mm)		**Weld depth (mm)**	
				Exp.	**Model**	**Exp.**	**Model**
1	1000	100	No	1.09	1.10	0.37	0.40
	1000	400	No	1.42	(-)	0.29	(-)
	1000	800	No	1.68	(-)	0.22	(-)
	1350	100	No	1.14	1.20	0.40	0.53
	1500	100	No	1.30	1.26	0.51	0.67
	1750	100	No	1.42	1.29	0.79	0.75
	2000	100	No	1.45	1.40	1	1
	3000	100	No	1.84	1.63	1	1
2	1400	25	No	(-)	(-)	(-)	(-)
	4000	25	Yes	1.97	(-)	2	(-)
	4000	50	No	1.83	(-)	2	(-)
	4000	100	Yes	1.47	1.57	2	2
	4000	200	yes	(-)	(-)	(-)	(-)
5	1400	16.9	Yes	2.88	(-)	2.43	(-)
	1400	25	Yes	(-)	(-)	(-)	(-)
	4000	25	Yes	2.86	(-)	5	(-)
	4000	50	Yes	2.85	(-)	5	(-)
	4000	100	Yes	1.52	(-)	5	(-)

Table 5: Pore analysis results performed using the X-ray tomography measurements made along the weld. Note that maximum pore diameter has been reported here.

Welding condition			**Pore analysis**				
Plate thickness (mm)	**Laser power (W)**	**Traveling speed (mm/s)**	**Probability (%)**	**Diameter (mm)**	**Volume (mm^3)**	**Surface (mm^2)**	**No of pores**
2	4000	25	3.05	0.83	0.2	3.98	1
2	4000	50	0	0	0	0	0
2	4000	100	0.74	0.38	> 0.1	0.34	1
5	1400	16.9	10.87	1.16	0.23	4.18	5
5	4000	25	15.12	1.04	0.31	4.75	7
5	4000	50	2.36	0.84	0.05	4.35	5
5	4000	100	0.59	0.91	0.07	3.93	1

Video Captions

Click here to download Supplementary Material: VideosR1.docx

Unpublished manuscript

Click here to download Supplementary Material: UnpublishedManuscript.pdf

*Graphical Abstract

Graphical Abstract

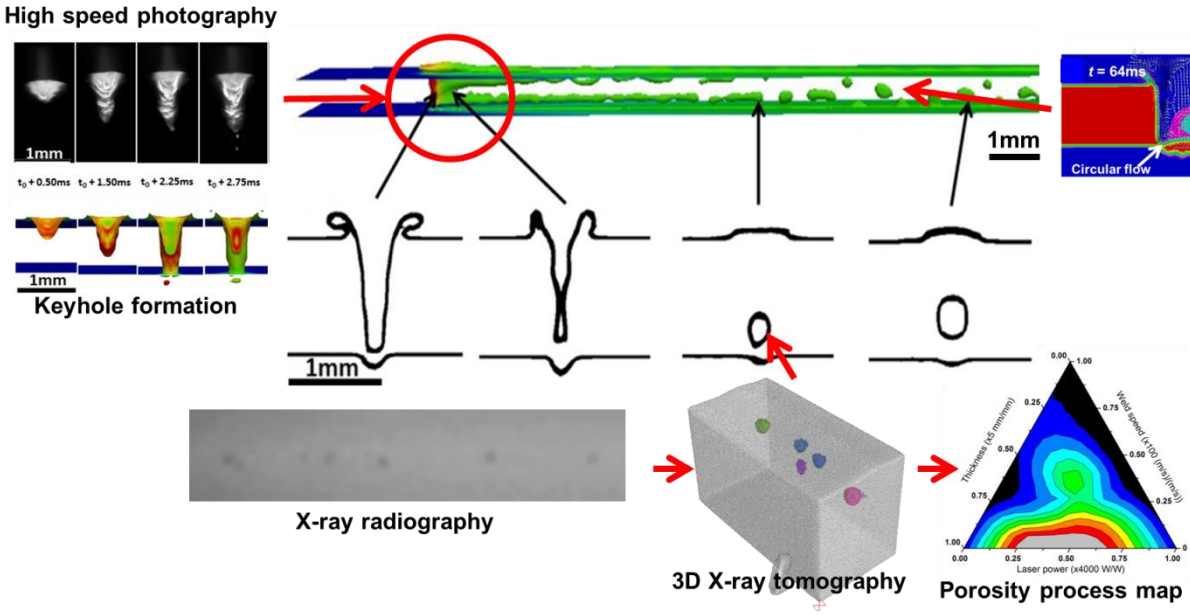

Video Still 1

Click here to download high resolution image

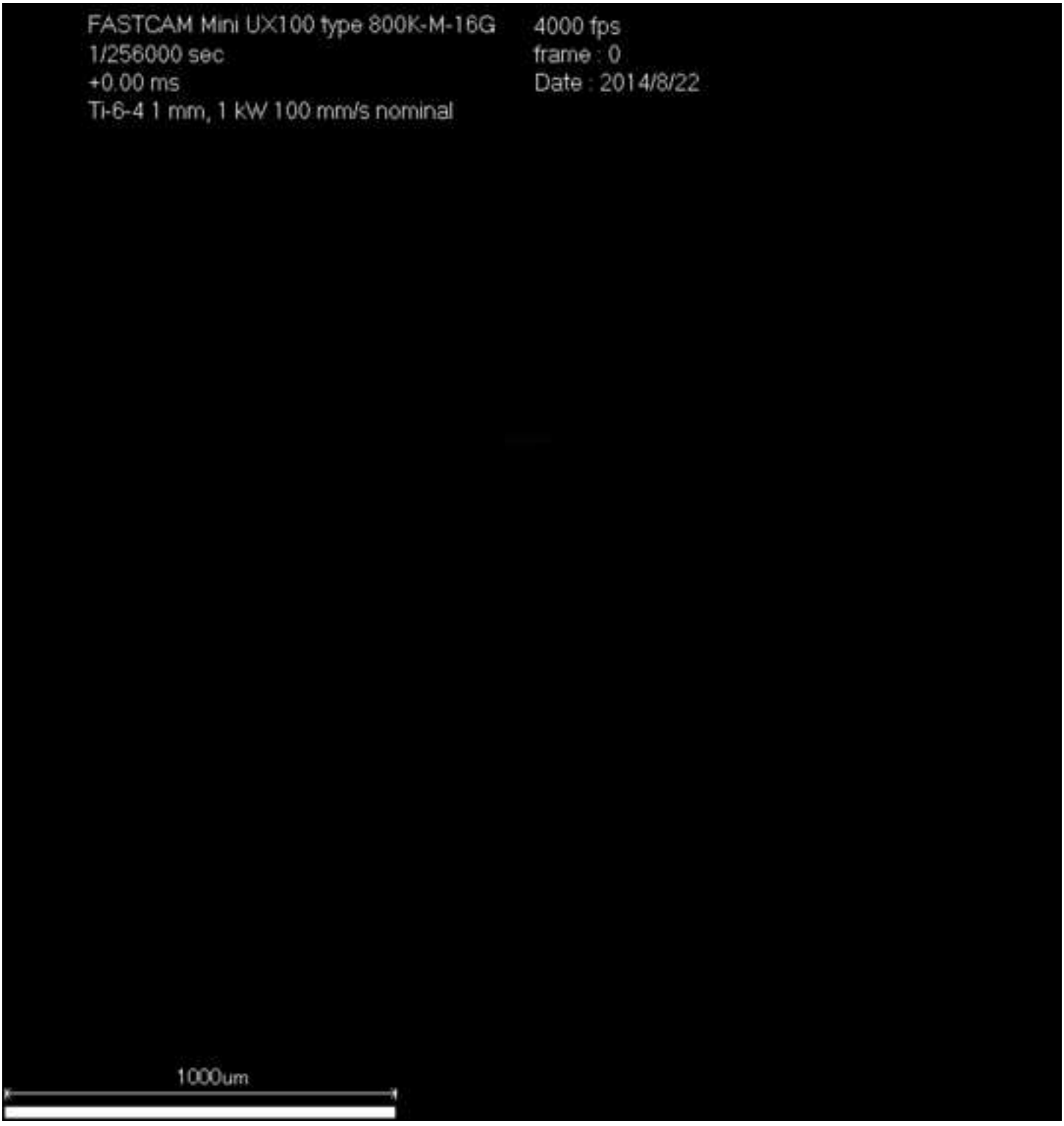

Video Still 2

Click here to download high resolution image

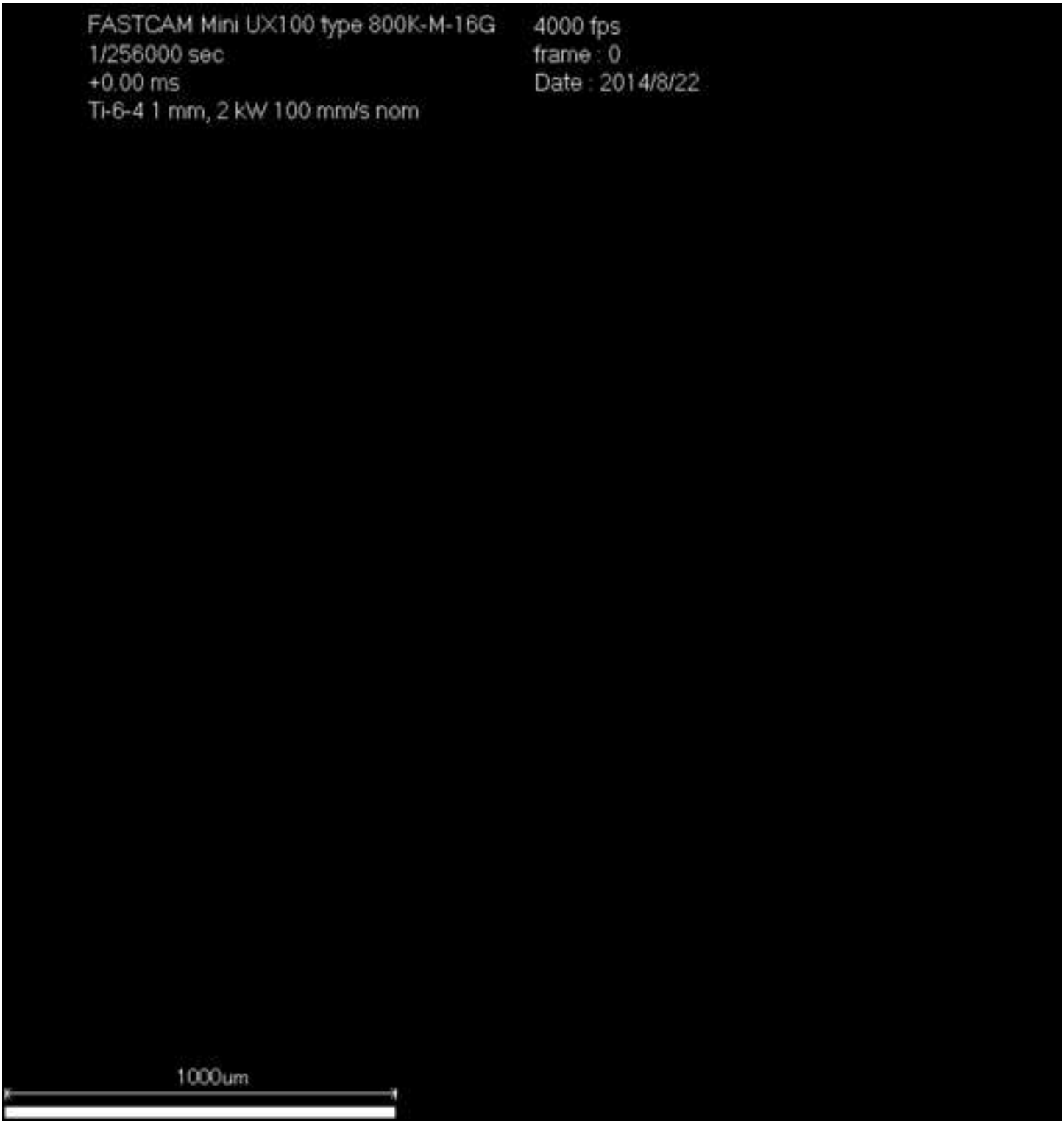

Video Still 3

Click here to download high resolution image